Acta Materialia 116 (2016) 14–28

Contents lists available at ScienceDirect

Acta Materialia

journal homepage: www.elsevier.com/locate/actamat

Full length article

Additively-manufactured metallic micro-lattice materials for high specific energy absorption under static and dynamic loading

Thomas Tancogne-Dejean [b], Adriaan B. Spierings [c], Dirk Mohr [a, *]

[a] Department of Mechanical and Process Engineering, ETH Zurich, Switzerland
[b] Impact and Crashworthiness Laboratory, Department of Mechanical Engineering, Massachusetts Institute of Technology, Cambridge MA, USA
[c] Innovation Centre for Additive Manufacturing (icams), INSPIRE-AG, St. Gallen, Switzerland

ARTICLE INFO

Article history:
Received 17 May 2016
Accepted 30 May 2016
Available online 18 June 2016

Keywords:
Octet truss lattice
Specific energy absorption
Additive manufacturing
Split Hopkinson bar testing
Finite element analysis

ABSTRACT

An octet truss lattice material is designed for energy absorption purposes featuring an exceptionally high specific energy absorption, a constant plateau stress between initial yield and densification, and zero plastic Poisson's ratio. It is demonstrated through detailed finite element simulations that the meso-structural response of metallic lattice materials under compression changes from an unstable twist mode to a stable buckling free mode at a relative density of about 0.3. Furthermore, it is found that the nature of the macroscopic stress-strain curve changes from mildly-oscillating to monotonically-increasing as the meso-structural deformation mode changes, while a stress-plateau is observed at relative densities above 0.3. Since the specific energy absorption is a monotonically increasing function of the relative density, lattice materials of relative densities around 0.3 feature both a plateau stress and a high specific energy absorption capability. Prototype materials are built from stainless steel 316L using Selective Laser Melting. The basic building element of the micro-lattices are 2.2 mm long beams with a 500 μm diameter cross-sections. Detailed micro- and meso-structural analysis including tomography, microscopy and EBSD analysis revealed substantial local material property variations within the lattice structure. Compression experiments are performed under static and dynamic loading conditions confirming the anticipated exceptional energy absorption material characteristics for strain rates of up to 1000/s.

1. Introduction

Truss lattice materials are man-made open porous cellular solids with periodic truss microstructures. In essence, these are space-filling 3D networks made from hollow or solid truss elements. Depending on their nodal connectivity, the mechanical response of highly porous truss lattice materials may be described as either bending-dominated or stretching-dominated [1]. With recent progress in micro- and nano-fabrication technology, lattice materials can now be made with truss diameters ranging from the submicron to the millimeter level (e.g. Ref. [2]). Direct laser writing and additive manufacturing techniques provide an excellent control over the lattice geometry, thereby enabling the fabrication of almost any open porous truss architecture. At the same time, important scale effects in the parent material may be leveraged by reducing the characteristic structural dimensions. For example [3], built copper micro lattices with truss diameters of a few microns only that were stronger than fully-dense pure copper. [4] reported a size-effect in the stiffness and strength of alumina when coating a polymer lattice template. [5] demonstrated that hollow Al_2O_3 and Ni-P micro lattices provide a nearly constant stiffness per unit mass density over three orders of magnitude of density. Even at effective densities of only a few mg/cm^3, the Young's modulus to density ratio of microlattice materials is still close that of fully-dense metals.

The octet truss lattice architecture plays a central role in the above works as it is a statically-determinate space-filling Platonian solid which exhibits stretching-dominated meso-structural response. Even though the mechanical properties of the parent material may be size dependent, results regarding the deformation response of the octet truss lattice are applicable to lattice structures at the micron, millimeter and centimeter scale. Building on the early work of [6], [7] derived analytical estimates of the basic macroscopic mechanical properties of the octet truss lattice material. A multi-surface plasticity model for ideal octet truss lattice

* Corresponding author.

http://dx.doi.org/10.1016/j.actamat.2016.05.054
1359-6454/

materials has been derived by Mohr [8]; while a general computational homogenization approach for describing the non-linear constitutive response of lattice materials has been presented by Vigliotti et al. [9]. Messner et al. [10] made use of Bloch wave theory and detailed finite element calculations to derive a continuum model representing long-wavelength wave propagation in truss lattice materials.

Wadley and co-workers developed innovative manufacturing processes to make lattice materials from wire grids and sheet material (e.g. Refs. [11–13]). Knowing that the truss waviness knocks down both the stiffness and strength (e.g. Ref. [14]), special attention was paid to manufacturing lattice structures with minimal initial truss curvature. Many recent studies now rely on additive manufacturing for making metallic truss lattice materials. [15] produced stainless steel 316L Body-Centered-Cubic (BCC) lattice specimens with strut diameters of 210 μm and relative densities ranging from 4% to 14%. They report a significant loss in the basis material stiffness and strength related to defects introduced through Selective Laser Melting (SLM). Furthermore, their results confirm that the compressive response of BCC lattices is bending dominated, as expected from their detailed finite element simulations. In a second study on SLM made 316L lattices [16], they found that the manufacturing related lattice defects has a particularly harmful effect on the material properties under shear loading. Drop tower impact experiments on sandwich panels by Mines et al. [17] revealed that SLM made Ti-6Al-4V BCC lattices can match the performance of aluminum honeycombs. The analysis of dynamic compression experiments at a nominal strain rate of about 1000/s on tetrahedral aluminum truss core structures with 13.4 mm long and 1.5 mm thick struts suggests that strut buckling is delayed due to inertia effects [18].

Selective laser melting of a Ti-rich TiNi shape memory alloy has been employed by Li et al. [19] to create an auxetic lattice material. Their results clearly demonstrate the important effects of the SLM process parameters on the resulting parent material structure. Electron beam melting (EBM) provides an alternative to SLM with potentially higher production speeds, but the surface quality provides only little immediate improvements over that obtained through SLM [20], [21] created Ti-6Al-4V cubic and diamond lattice structures of relative densities of up to 17% using EBM. Their static and dynamic compression experiments show progressive crushing from the specimen boundary under static loading conditions and random cell layer collapse of the re-entrant cube lattice under dynamic loading.

From a strength perspective, lattice structures with hollow trusses (e.g. Ref. [22]) provide a higher load carrying capacity per unit density due to the higher second moment of inertia in comparison to solid round cross-sections. Design maps for octet truss architectures with struts of non-circular cross-sections have been developed by Elsayed and Pasini [23] to ensure that elastic buckling and plastic yielding occur simultaneously. The potential of hollow micro-lattices for energy absorbing systems is reemphasized by Evans et al. [24]. They show that the specific energy absorption of hollow truss lattices is even higher than that of honeycombs for the same relative density and basis material.

The space of potentially interesting truss lattice geometries is vast. Among other aspects, the design of a truss lattice material involves (a) the choice of the basis material, (b) the choice of the lattice geometry, e.g. cubic, tetrahedral, octet, etc., (c) the choice of the strut shape, and (d) the choice of the relative density of the lattice material. Here, an attempt will be made to keep the unit cell size of the truss material as small as possible to generate a lattice material, which can be treated as a homogeneous solid in standard engineering applications (e.g. energy absorption structures for transportation vehicles, jet engine components, etc.). By limiting our attention to additive manufacturing with metals, this design objective led us to 316L stainless steel as basis material. As compared to other powder materials such as aluminum or titanium alloys, struts of only 500 μm diameter can be manufactured from stainless steel while maintaining reasonable geometric accuracy.

Among different lattice geometries, we chose the octet truss lattice configuration as it provides a nearly isotropic elastic response. It features a unit cell composed of two Platonic solids: the tetrahedron and the octahedron (Fig. 1a). By definition of a Platonic solid, all struts have the same shape and length L. Its configuration resembles to a Face-Centered Cubic (FCC) crystal when the struts are considered as the shortest distance of atom-to-atom interaction. The surrounding light green cube in Fig. 1a represents the macroscopic volume filled by the octet lattice unit cell. The remaining open design questions, the choice of strut shape and relative density, will be determined through a parametric finite element study. The main criterion for selecting the "optimal" configuration will be the material's energy absorption characteristics: (1) constant stress plateau and zero plastic Poisson's ratio to allow for a constant deceleration of an impacting rigid mass, and (2) high specific energy absorption, i.e. the plastic work performed in the plateau regime under uniaxial compression shall be maximized for a given effective material density.

In the present work, we firstly carry out a parametric finite element study to identify the optimal relative density for which the compressive response of a stainless steel 316L octet truss lattice material achieves the above design objective. In particular, we determine the effect of the relative density and truss cross-section variations on the macroscopic stress-strain response for uniaxial compression. Subsequently, truss lattice specimens of a relative density of about 30% are manufactured and subjected to compression under static and dynamic loading conditions. In addition, the stainless steel 316L basis material is characterized under compression for strain rates of up to 1000/s. It is demonstrated both numerically and experimentally that an octet truss lattice material of a relative density of 30% is free from any initial peak stress and exhibits the ideal engineering stress plateau of an energy absorption material prior to densification. Furthermore, it is shown that the specific energy absorption of the tested material is significantly higher than that of conventional hexagonal honeycomb.

2. Analytical preliminaries

2.1. Relative density

The relative density $\bar{\rho}$ is defined by the ratio of the macroscopic

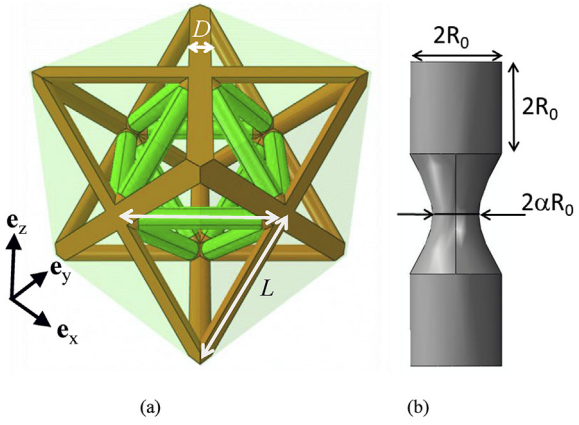

Fig. 1. (a) Unit cell of the octet truss lattice material, (b) geometry of a single strut.

density of a cellular solid and the density of the basis material,

$$\overline{\rho} = \frac{\rho}{\rho_s}. \tag{1}$$

For an octet lattice material with cylindrical stuts of radius R and length L, an approximate analytical relationship can be given for low relative densities [7],

$$\overline{\rho} = 6\sqrt{2}\pi\left(\frac{R}{L}\right)^2. \tag{2}$$

At high relative densities, the complex geometry of the strut joints needs to be taken into account when calculating the relative density. A curve fit of the relative densities calculated using a CAD software suggests adding a cubic correction to (2),

$$\overline{\rho} = 6\sqrt{2}\pi\left(\frac{R}{L}\right)^2 - C\left(\frac{R}{L}\right)^3 \tag{3}$$

with the coefficient $C = 54.6$.

2.2. Elastic response

The octet lattice material has cubic symmetry and its elastic response is thus described through three elasticity constants. In the $\{\mathbf{e}_x,\mathbf{e}_y,\mathbf{e}_z\}$ material coordinate system (Fig. 1a), the elastic stress-strain relationship may be written as

$$\begin{Bmatrix} \varepsilon_{xx} \\ \varepsilon_{yy} \\ \varepsilon_{zz} \\ 2\varepsilon_{xy} \\ 2\varepsilon_{xz} \\ 2\varepsilon_{yz} \end{Bmatrix} = \begin{bmatrix} 1/E & -\nu/E & -\nu/E & 0 & 0 & 0 \\ & 1/E & -\nu/E & 0 & 0 & 0 \\ & & 1/E & 0 & 0 & 0 \\ & & & 1/G & 0 & 0 \\ & sym & & & 1/G & 0 \\ & & & & & 1/G \end{bmatrix} \begin{Bmatrix} \sigma_{xx} \\ \sigma_{yy} \\ \sigma_{zz} \\ \sigma_{xy} \\ \sigma_{xz} \\ \sigma_{yz} \end{Bmatrix} \tag{4}$$

with the Young's modulus E, the elastic Poisson's ratio ν, and the shear modulus G. For the octet truss lattice with cylindrical struts [1,7], proposed the analytical forms

$$\frac{E}{E_s} = \frac{\overline{\rho}}{9} \tag{5a}$$

$$\nu = \frac{1}{3} \tag{5b}$$

$$\frac{G}{G_s} = \frac{1+\nu_s}{6}\overline{\rho} \tag{5c}$$

to estimate the lattice moduli as a function of the relative density $\overline{\rho}$ and the elastic constants $\{E_s,\nu_s\}$ of the basis material.

2.3. Specific energy absorption

The Specific Energy Absorption (SEA) ψ is defined as the work W performed per unit weight when the material is compressed in a uniaxial manner up to a strain of -0.3,

$$\psi := \frac{W}{\rho} \text{ with } W = \int_0^{-0.3} \sigma d\varepsilon \tag{6}$$

with ρ denoting the mass density, σ the axial stress and ε the work-conjugate axial strain.

3. Experimental procedures

3.1. Material fabrication

Micro lattice materials are manufactured on an SLM machines from Concept Laser, type M1. The machine is equipped with a disk laser with 100 W (effective beam diameter approx. 150 μm), operated in cw-mode. A standard scanning strategy is applied where 5×5 mm^2 islands are scanned in a random sequence. The most relevant processing parameters are summarized in Table 1. These parameters are expected to result in a material density of about 99% ± 0.2% (as measured previously on $10 \times 10 \times 10$ mm^3 cubes). As the material density is dependent on the cooling history of the melt-pool (which is structure-dependent), some variations from this target density may occur. To account for the low thermal conductivity of lattice structures during laser scanning, the scan speeds applied to manufacture these structures are increased by about 10% as compared to normal scan speeds. The characteristic metrics of the SS316L powder particle size distribution are given in Table 1. After manufacturing, the samples are cleaned using standard blasting equipment (Peenmatic-Micro 620S9) with steel balls type MS/Z350B at an air pressure of 4 *bars*.

3.2. Meso- and microscopic characterization

The specimen dimensions are measured after manufacturing using a 1 μm precision caliper. The density of the basis material is measured using Archimedean's method with ethanol as wetting liquid. The geometry of the manufactured specimens is also investigated using micro-computed tomography with a voxel size of 18 μm. Microscopic observations are realized on a FEI Quanta 600 scanning electron microscope on raw (non-polished) samples. Electron Back Scatter Diffraction (EBSD) analysis is carried out on polished specimens to determine the crystal size and texture. Silicon carbide abrasive paper and 3 μm diamond paste are used for mechanical polishing. Final polishing is made using alumina silica with acid.

3.3. Mechanical experiments

3.3.1. Specimens

- *Cubic lattice specimens* of an edge length of about 21.5 mm are used for static and dynamic compression testing of the lattice material along the build direction.
- *Mini-cylinder specimens* with their axis parallel to the build direction are directly made through selective laser melting. The manufactured specimens have an initial diameter of 0.92 mm and a height of 1.83 mm. They are manufactured along with an 8.9 mm diameter cylindrical base as an integral part. The residual non-molten powder is removed from the specimen

Table 1
SLM processing parameters for stainless steel 316L (Concept Laser M1).

Layer thickness [μm]	30
Laser power [W]	100
Scan speed [mm/s]	475
Hatch distance [μm]	130
Specific energy density [J/mm^3]	54
Particle size distribution values in [μm]	$q_{10} = 9.2$ $q_{50} = 12.8$ $q_{90} = 21.6$ $Q_{10} = 12.2$ $Q_{50} = 22.8$ $Q_{90} = 42.6$

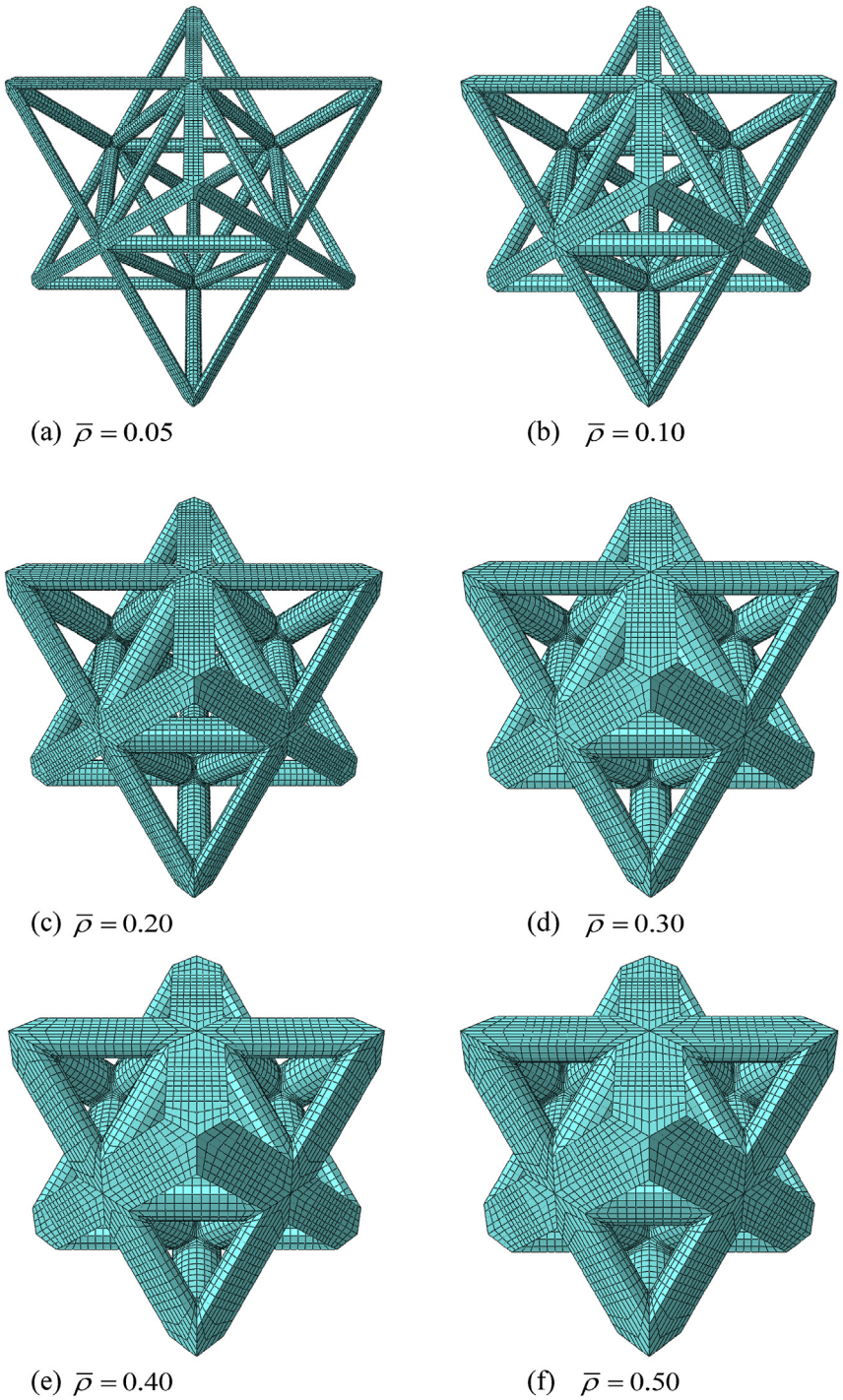

Fig. 2. FE meshes of octet truss lattice configurations with cylindrical struts of different relative densities.

surface through polishing on a lathe with abrasive paper. The final diameter of the specimen is thereby reduced to 0.81 mm. At the same time, the specimen is shortened to 1.44 mm length.

- *Standard cylinder specimens* of 8.9 mm diameter and 7.8 mm length are also directly made through selective laser melting. Analogously to the mini-specimens, the specimen axis is aligned with the build direction.
- *Ring specimens* for dynamic testing: the standard cylinder specimens are further shorted to 3.5 mm length. At the same time, a hole is introduced into the specimen to ensure a uniaxial stress state, resulting in a stocky tubular specimen of 6 mm inner diameter and 8.9 mm outer diameter.

3.3.2. In-situ SEM uniaxial compression testing procedure

In-situ compression experiments on the 1.83 mm long mini-cylinder specimen are carried out using a custom-made screw-driven loading device in the FEI Quanta 600 Scanning Electron Microscope (SEM). The testing speed is 1 μm/s which corresponds to a strain rate of 8×10^{-4}/s. SEM images are taken for Digital Image Correlation (DIC) at 30 μm and 60 μm displacement increments at a

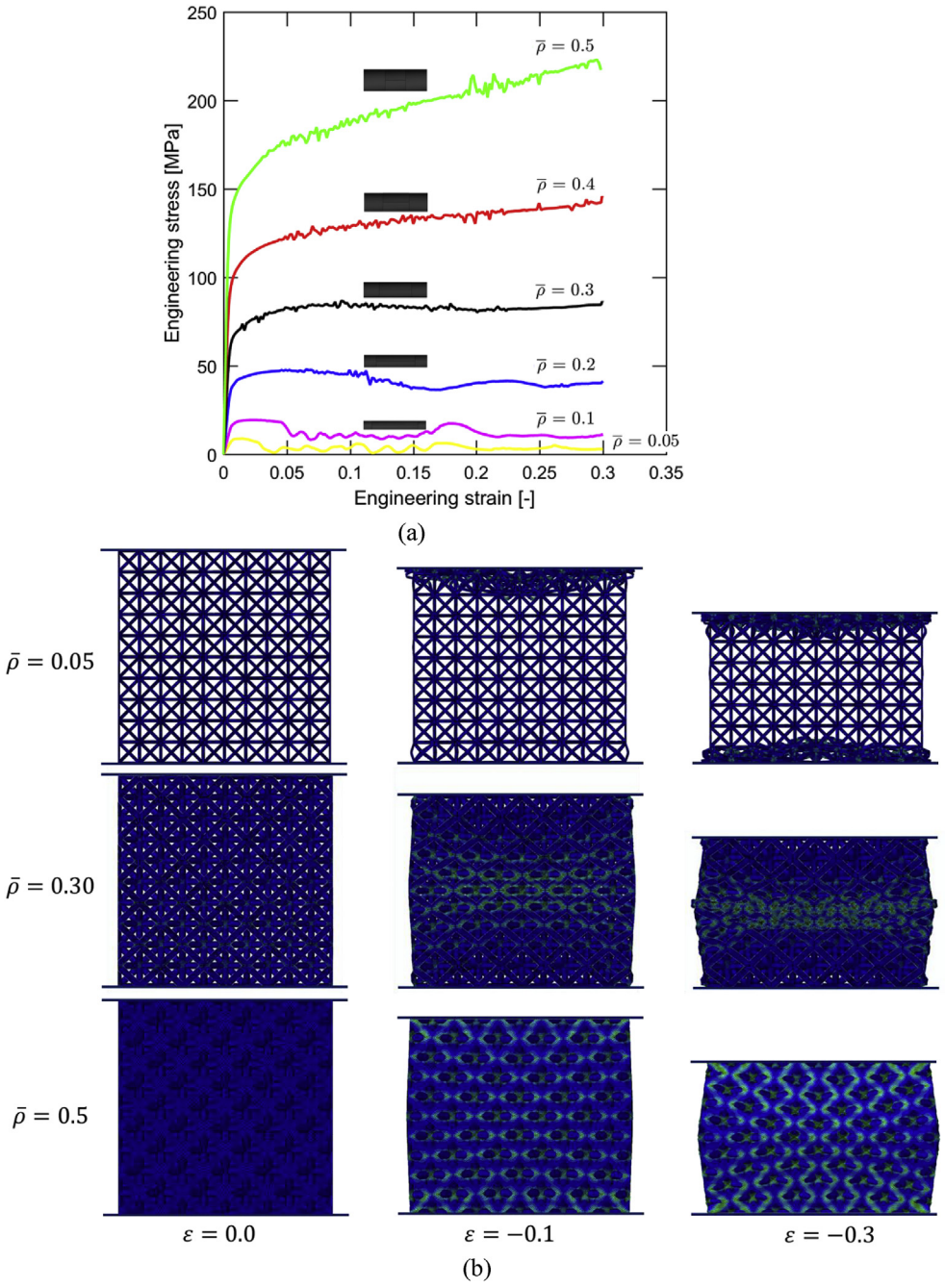

Fig. 3. Macroscopic response of the octet truss lattice under uniaxial compression: (a) Macroscopic stress-strain curves for different relative densities, (b) corresponding side views of the deformed finite element meshes showing the local equivalent plastic strain as contour.

resolution of 0.41 μm per pixel. The natural contrast of the specimen surface is used as random pattern for Digital Image Correlation (DIC) strain measurements. In particular, we report the axial strains that are computed using a virtual extensometer of 1.25 mm length.

3.3.3. *Macroscopic compression experiments on universal testing machine*

The standard cylindrical specimens and the cubic lattice specimens are tested on a hydraulic MTS testing machine equipped with two parallel high strength steel loading platens. As for the mini-specimens, the surface roughness of the standard specimens is used as a random pattern to measure the surface displacement through DIC with the software VIC2D (Correlated Solutions). The images are acquired at a frequency of 1Hz using an AVT Pike F-505B camera with a Tamron 90 mm 1:1 macro lens. Experiments are performed at a constant cross-head speed of 0.6 mm/min which equates to an axial strain rate of about 10^{-3}/s. The axial strains are computed using a virtual extensometer length of 6.5 mm.

The static experiments on the cubic lattice specimens are performed at a constant cross-head velocity of 1 mm/min. Here, the relative displacement of the specimen boundaries is determined through the DIC tracking of a random speckle pattern on the loading platens. Photographs of the entire specimen are taken using the same optical system as above at a frame rate of 1 Hz to

monitor the deformation mode of the lattice structure.

3.3.4. Split Hopkinson Pressure Bar (SHPB) testing technique

The high strain rate experiments are performed on modern Split Hopkinson Pressure Bar (SHPB) systems. A steel system is used to test the basis material ring specimens, while a larger diameter aluminum specimen is employed for the cubic lattice specimens:

- Steel SHPB system: All the bars are made of hardened maraging steel and have a diameter of $D_H = 20$mm. The input, output and striker bar lengths are $L_{in} = 2.89$m, $L_{out} = 2.01$m and $L_{st} = 1.20$ m, respectively. The output bar strain gage is positioned at a distance of 365 mm from the output bar-specimen interface. The recordings of a second strain gage positioned near the center of the input bar (at a distance of 1444 mm from the input bar-specimen interface) are used together with those of the output bar strain gage to determine the relative displacement of the specimen boundaries. Standard formulas (e.g. [28]) for the wave transport are employed to determine the force history at the output bar-specimen interface and the relative displacement of the specimen-bar interfaces.
- Aluminum SHPB system with 40 mm diameter bars. The length of the input and output bars is $L_{in} = L_{out} = 2.50$ m and the striker length is $L_{s\,t} = 0.865$ m. The resulting duration of an experiment without wave superposition in the input bar is 490μs. At a strain rate of 1000/s, the maximum achievable strain within this duration would thus be 0.49. To increase the valid measurement time, we make use of three strain gages on the input and output bars (the strain gages on the input bar are located at a distance of 1.25 m, 1.273 m and 2.148 m from the specimen, while the output bar gages are located at a distance of 0.34 m, 0.39 m and 0.975 m from the specimen). A deconvolution algorithm [25] is then employed to calculate the force history at the output bar-specimen interface and the relative displacement of the specimen-bar interfaces.

Note that wave dispersion is taken into account when "transporting" the waves in the Hopkinson bars (using the DAVID SHPB signal processing software). The true stress-strain curve is then computed from the force and displacement histories using conventional formulas. A high speed camera (Phantom v7.3) is employed to monitor the lattice specimen deformation mode at a frequency of about 50 kHz.

4. Finite element modeling

4.1. Basis material model

The basis material stainless steel 316L is modeled using a simple rate-independent J2-plasticity model with isotropic hardening, thereby neglecting the possible effect of anisotropy, rate dependency, kinematic hardening and martensitic phase transformation. We assume a Young's modulus of 210 GPa and a Poisson's ratio is 0.3. A piece-wise linear hardening curve is calibrated based on earlier tensile experiments on SLM-made specimens [27]. The hardening behavior is highly non-linear until a stress of 733 MPa is reached at a strain of 0.05, subsequently, it hardens in an approximately linear manner with a tangent modulus of 1077 MPa. The assumed hardening behavior corresponds to the average of the stress-strain curves obtained from experiments on specimens where the loading direction corresponded to the build direction (vertical), and to the in-plane (horizontal) direction.

4.2. Lattice structure models

The finite element models are built to predict the large strain uniaxial compression response of octet truss lattice materials of different relative densities and strut shapes. Instead of using periodic boundary conditions on a single unit cell, we discretized a full specimen comprised of 5 × 5 × 5 unit cells using first-order solid elements (type C3D8R from the Abaqus library). All geometries

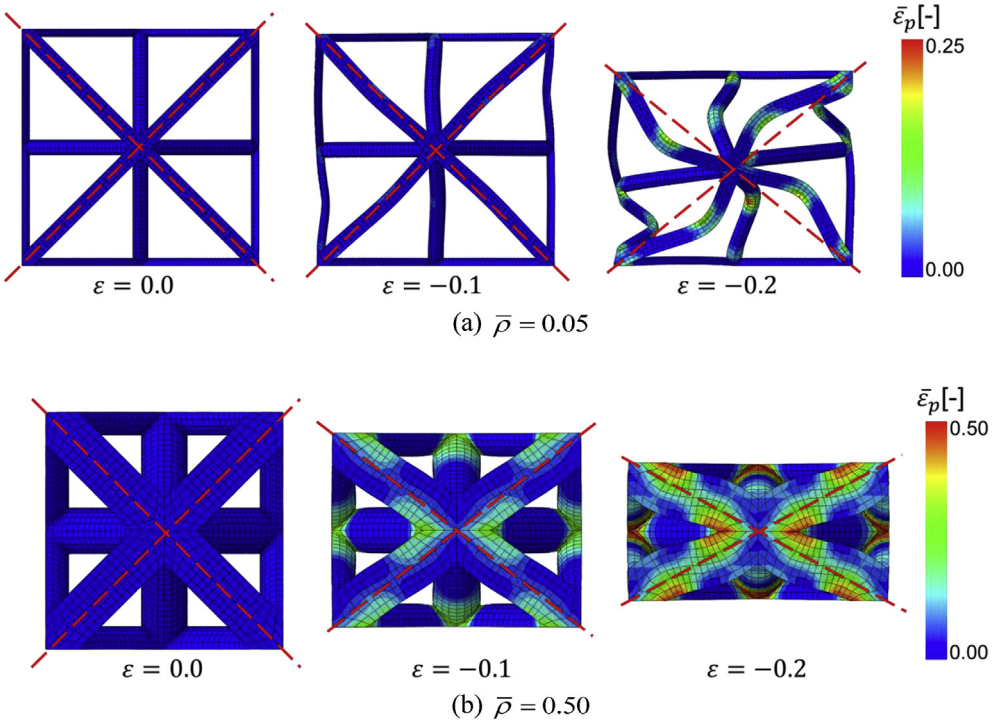

Fig. 4. Density-dependent unit cell deformation mode: (a) twist mode at low relative densities, (b) stable mode at high relative densities.

featured the same strut length of 2.18 mm, which corresponded to a unit cell edge length of 3.08 mm. To guarantee nearly isotropic elastic properties at the macroscopic level, we limit our attention to struts of circular cross-section (Fig. 1b). For all configurations, the strut ends are of cylindrical shape over a length of twice the strut radius R_0. Between these two end regions, the strut radius changes gradually in a parabolic manner reaching its extreme value of αR_0 at the strut center. The strut shape is therefore defined through the factor α, with $\alpha < 1$ describing notched configurations, $\alpha = 1$ describing a perfectly cylindrical configuration, and $\alpha > 1$ describing inversely-notched configurations.

In all meshes (Fig. 2), we chose approximately the same element size of 80 μm. The cubes are placed between two parallel rigid plates assuming a tangential friction coefficient of 0.1. The bottom plate

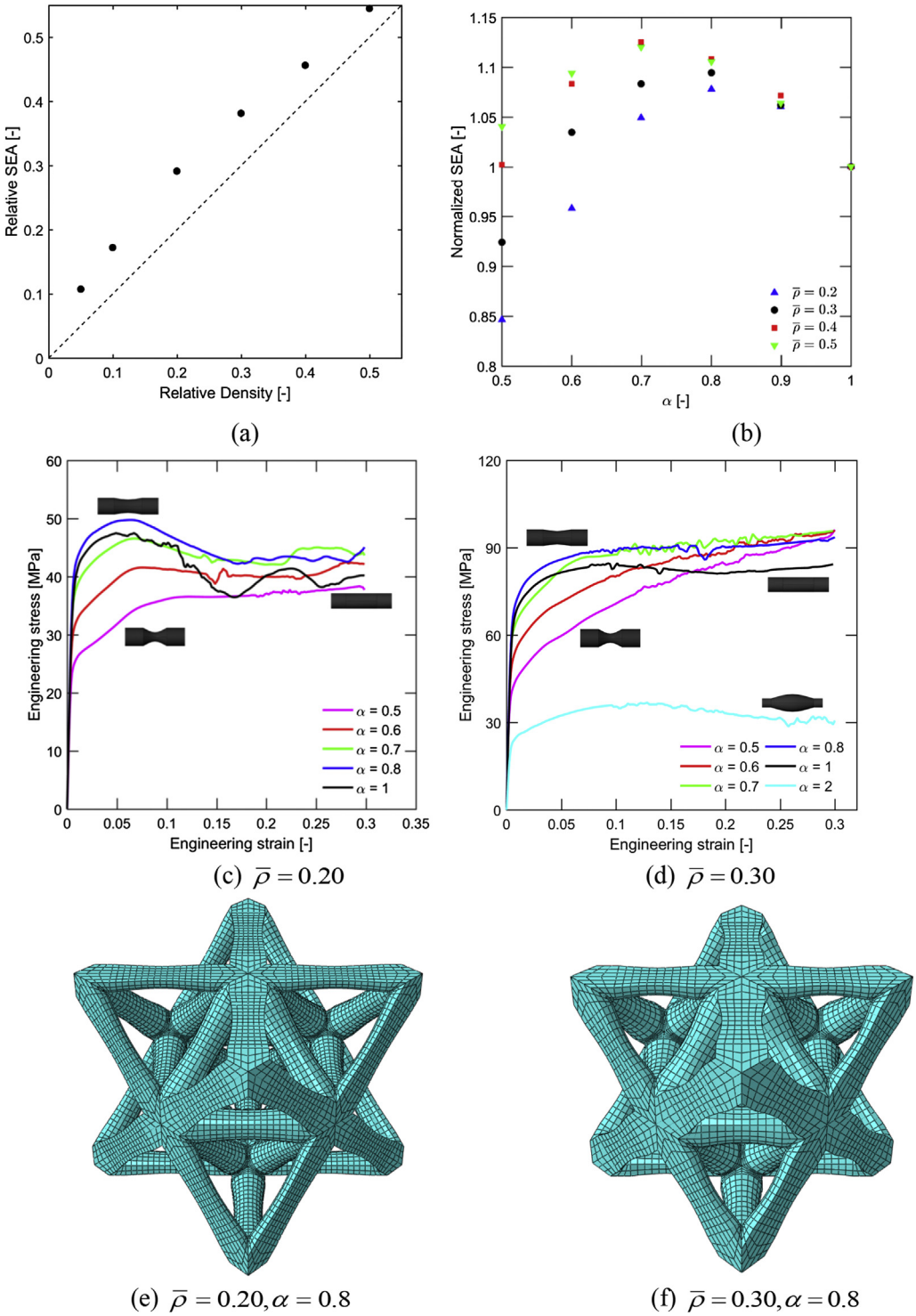

Fig. 5. Specific energy absorption of lattices (a) as a function of the relative density for $\alpha = 1$ (no taper), and (b) as a function of the reduction ratio α; stress-strain response and unit cell model (c, e) for $\overline{\rho} = 0.20$, and (d, f) for $\overline{\rho} = 0.30$.

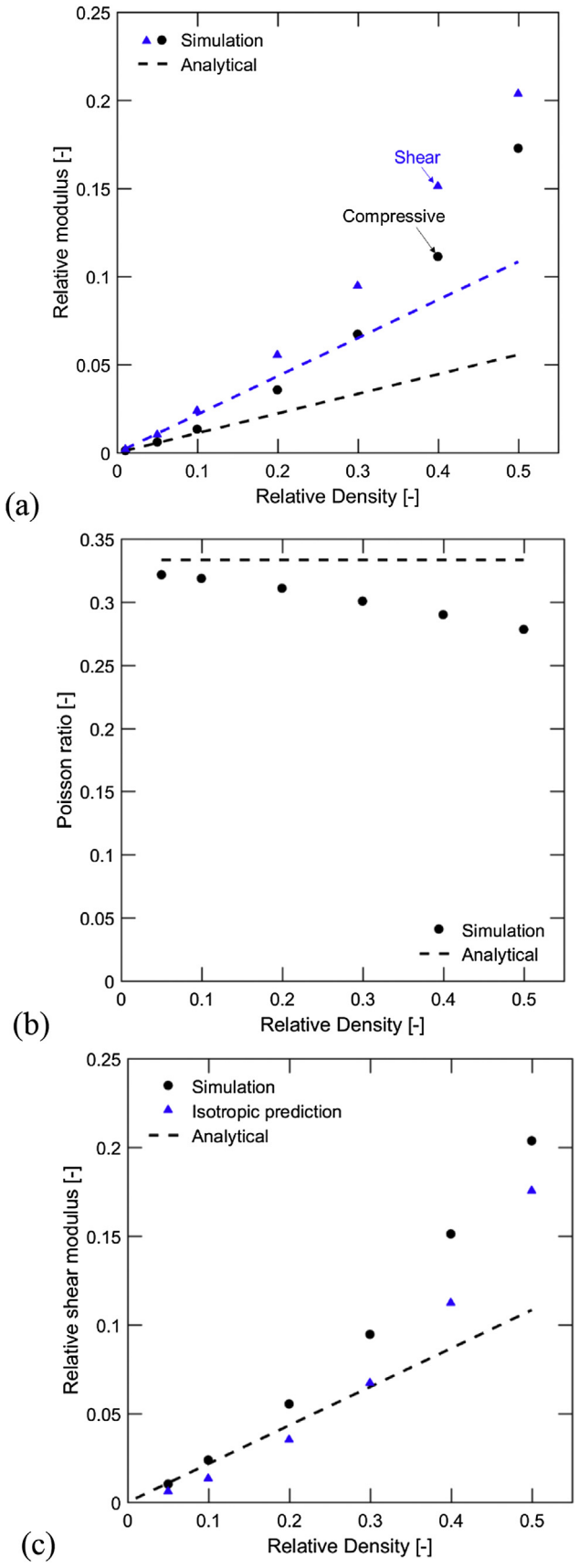

Fig. 6. Density-dependent response of the octet truss lattice material with cylindrical struts (a) Young's modulus, (b) elastic Poisson's ratio, and (c) shear modulus.

remained stationary while the top plate moved downward at a constant speed to compact the specimen by 30%. All simulations with the finite element software Abaqus/explicit (vers. 6.14–1) are performed on a high performance cluster in parallel mode on 120 CPUs.

5. Results

5.1. Computational study

5.1.1. Effect of relative density

A first series of simulations is concerned with the effect of the relative density on the compression response of micro lattice materials with perfectly cylindrical struts ($\alpha = 1$). Simulations are performed for $\overline{\rho} = \{0.05, 0.1, 0.2, 0.3, 0.4, 0.5\}$ which corresponded to strut diameters of $D = \{0.2, 0.29, 0.42, 0.53, 0.64, 0.74\}$ mm. The corresponding unit cell meshes are shown in Fig. 2. The results are reported in terms of the macroscopic engineering stress versus the axial engineering strain (Fig. 3a). For a relative density of 0.3, we observe a plateau-like behavior, i.e. the hardening slope of the macroscopic engineering stress-strain curve is close to zero. For relative densities greater than 0.3, an approximately linear positive hardening is observed, while a mildly-oscillating stress-strain response is observed for configurations of low relative density.

When comparing the meso-structural deformation modes of materials of different relative densities (e.g. 0.05, 0.3 and 0.5, see Fig. 3b), it can be seen that the low density material fails progressively from the specimen boundaries, a characteristic that has been widely observed for other conventional low density solids. The microstructural deformation mode for high relative densities is fundamentally different. As shown in the right column of Fig. 3b, the deformation is spread more uniformly over the entire specimen, with a slight concentration towards the specimen center where the lateral expansion of the lattice structure is not prohibited by the boundary conditions.

Fig. 4 provides a more detailed illustration of the fundamental difference between the microstructural deformation mechanisms in stable and unstable lattice configurations. In both cases, the highest plastic strains are found near the nodes which is consistent with simple analytical derivations for a beam network. However, slender struts buckle (elastically or plastically) under the axial load which results in the formation of an additional plastic hinge near the center of the struts (Fig. 4a). As the lattice structure is compressed further, most plastic deformation is concentrated in these newly-formed strut center hinges while the strut intersections seem to behave like rigid nodes. Instead of deforming, the latter undergo large rigid body rotations while the lattice structure is twisted. This "twist mode" is the characteristic feature of the unstable, low density structures. In contrast, the nodes of stable high-density lattices do not rotate (Fig. 4b). Instead, the struts form plastic hinges at the nodes. Due to the short node-to-node distance (as normalized by the strut diameter) in high density lattices, the plastic hinges of neighboring nodes interact with each other, thereby creating a continuous zone of plastic deformation throughout the struts.

We evaluated the dependency of the Specific Energy Absorption (SEA) on the relative density based on the above simulation results. In Fig. 5a, the results are shown as normalized by the SEA of the fully dense basis material, $\psi_s = 26.6\, J/g$. It is found that the SEA is a monotonically increasing function of the relative density, i.e. the denser the lattice material, the higher its weight specific energy absorption capability. In a first approximation, the relative SEA is proportional to the relative density (see dashed line in Fig. 5a),

Table 2
Lattice specimen dimensions and weight.

Specimen number	Build direction [mm]	x-direction [mm]	y-Direction [mm]	Mass [g]	Density [g/cm^3]	Relative density [–]
1	22.049	21.588	21.546	21.70	2.12	0.265
2	21.830	21.524	21.606	21.13	2.08	0.260
3	21.838	21.545	21.542	21.35	2.11	0.264
4	21.797	21.569	21.487	21.04	2.08	0.261
5	22.116	21.500	21.601	22.31	2.17	0.272
6	21.936	21.590	21.554	22.43	2.20	0.275
7	22.048	21.538	21.525	22.78	2.23	0.279
8	21.901	21.571	21.494	22.08	2.17	0.272
9	21.862	21.616	21.490	22.15	2.18	0.273
10	22.137	21.487	21.540	22.90	2.23	0.280
11	21.839	21.506	21.509	21.18	2.10	0.262
12	21.915	21.565	21.645	22.62	2.21	0.277
Average:	21.939	21.550	21.545	21.97	2.16	0.270
Std. dev:	0.119	0.0340	0.0501	0.671	0.0572	0.00716

$$\frac{\psi}{\psi_s} = \frac{\rho}{\rho_s}. \tag{7}$$

Since the SEA is already normalized by the density, the absorbed energy is actually a quadratic function in density,

$$W = \psi\rho = \left(\frac{\psi_s}{\rho_s}\right)\rho^2. \tag{8}$$

In other words, the energy absorption performance of a lattice material increases substantially for higher densities. From a mechanistic point of view, this may be explained through the growing meso-structural stability with relative density. When the deformation is highly localized at the meso-structural level, a

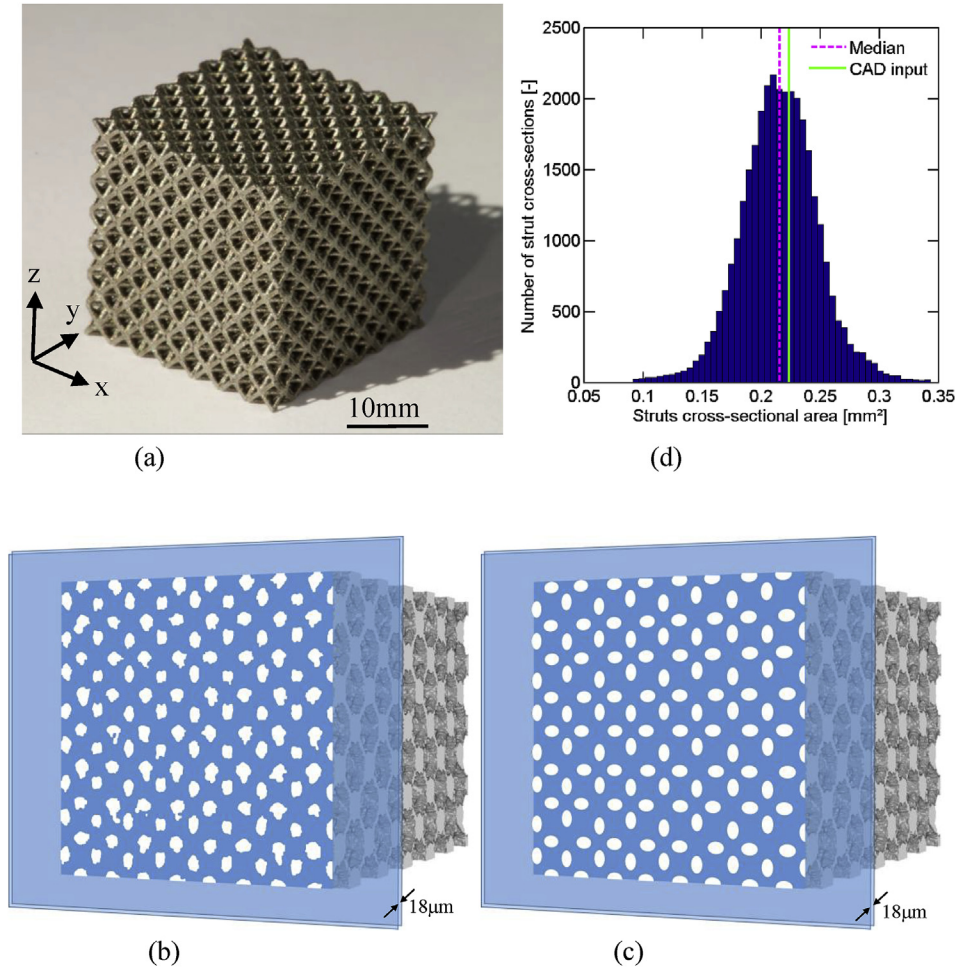

Fig. 7. (a) Photograph of a cubic lattice specimen, (b) tomography image with voxel edge length of 18 µm, (c) theoretical cross-sectional view of the lattice, (d) histogram of measured strut cross-section area.

significant portion of the lattice structure undergoes mostly rigid body motion only (such as the twist mode). This portion contributes to the overall weight of the lattice material even though it does not contribute to the energy absorbed. As discussed above, the plastic deformation becomes more wide-spread within the lattice structure, the shorter the normalized node-to-node distance L/D, which explains the increase in energy absorption efficiency as a function of the relative density.

Fig. 6a presents the evolution of the relative Young's modulus as function of the relative density as obtained from our simulation for cylindrical struts. Different from the analytical approximations for low density lattices, the elastic properties for relative density higher than 0.1 scale with a power exponent higher than 1. This difference is attributed to the importance of the effect of the strut joints on the mechanical response which is neglected in analytical derivations.

We also determined the Poisson's ratio and the shear moduli (Fig. 6b and c) using our finite element models. As for the Young's modulus, the analytical estimates (dashed curves) are valid for low relative densities. To evaluate the degree of anisotropy in the material, we also calculated the shear modulus using the well-known analytical relationship for isotropic materials,

$$G_{iso} = \frac{E}{2(1+\nu)} \tag{9}$$

The comparison of the isotropic shear modulus estimate (blue dots) with that obtained computationally (black dots) shows convergence as the relative density increases. In other words, the higher the relative density of the octet truss lattice material, the lower its degree of elastic anisotropy.

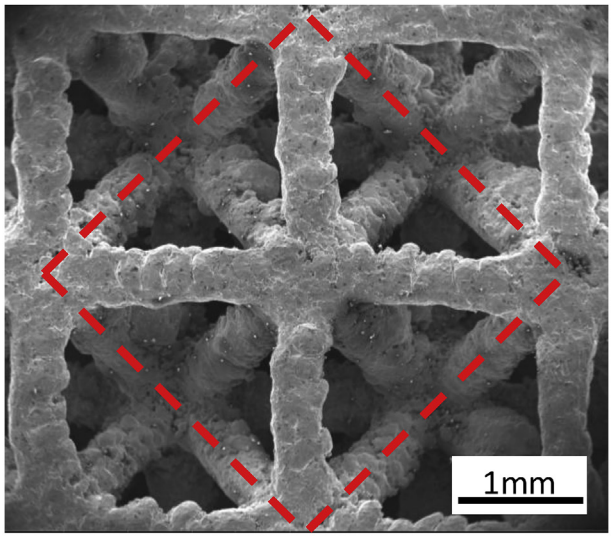

Fig. 8. SEM observations on unpolished sample: (a) top view of a unit cell (interior of dashed area), (b) detail of nodal region.

5.1.2. Effect of strut geometry

We repeated the above simulations for lattices with struts that feature a larger ($\alpha > 1$) and a smaller ($\alpha < 1$) diameter at the center than at the strut ends (recall definition of α from Fig. 1b). As shown in Fig. 5c and d for relative densities of 0.2 and 0.3, respectively, the strut shape can change the nature of the overall stress-strain response from monotonically increasing to mildly-oscillating. It appears that strongly tapered struts ($\alpha \leq 0.6$) increase the stability of the microstructure at the expense of a lower macroscopic strength. The highest SEA for a given relative density is always observed for $\alpha \cong 0.8$ (Fig. 5b). The corresponding lattice unit cells are shown in Fig. 5e and f. However, the relative increase as compared to cylindrical struts ($\alpha = 1$) is usually smaller than 10%. Increasing the strut diameter at the center ($\alpha > 1$) suppresses the twisting mode, but it also enforces the localization of deformation at the lattice nodes which resulted in a poor strength and energy absorption capability.

5.2. Experimental study

The main conclusions from our computational study are (1) that the energy absorption of lattice materials with cylindrical struts shape is among the highest of all shapes considered, and (2) that the meso-structural deformation mechanism changes from stable to unstable at a relative density of about 0.3, where the material deforms at nearly constant stress level prior to densification. In view of developing low density lattice materials with a plateau-like response for energy absorption purposes, our experimental study focusses on SLM-made octet truss lattice prototype material with cylindrical struts and a target relative density of 0.3. Using the same strut length (node-to-node distance) of $L = 2.18$ mm in both the experiments and simulations, a strut diameter of 534 µm is targeted in the additive manufacturing process to obtain a relative density of 0.3 according to Eq. (3).

5.2.1. Meso- and microstructural analysis of the prototype material

The target geometry for the lattice specimens (CAD input for the SLM machine) is a perfect cube comprised of $7 \times 7 \times 7$ unit cells ($21.56 \times 21.56 \times 21.56$ mm^3). However, our measurements (Table 2) reveal that the specimen height (average of 21.94 mm) is systematically greater by about 2% than the specimen in-plane dimensions (average of 21.55 mm). The average specimen mass is 21.97 g with a standard deviation of 3%. The measured density of the solid strut material is 7960kg/m3. The comparison with the density for stainless steel 316L reported in the literature indicates a microporosity of 0.8% inside the struts. The resulting average relative density of the lattice structure is $\overline{\rho} = 0.27$, which is about 10% smaller than its manufacturing target value.

Fig. 7b shows a representative micro-computed tomography image of a cubic lattice specimen. The dimensional accuracy is evaluated through vertical slices. The shape of the strut cross-

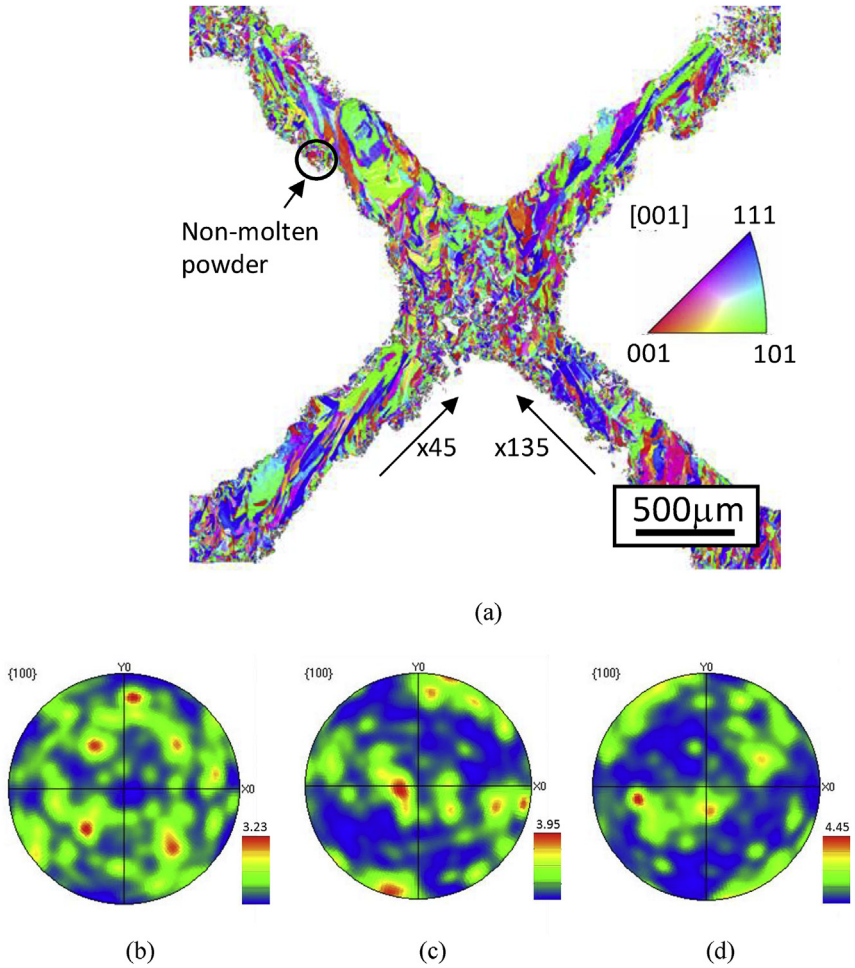

Fig. 9. EBSD analysis of polished sample: (a) grain structure with [001] crystal plane orientation contour. Inverse pole figures for (b) non-molten powder, (c) the ×45 strut, and (d) the ×135 strut.

sections seen in the μCT slices deviate significantly from the ideal periodic array of elliptical cross-sections of the target geometry (shown schematically in Fig. 7c). Fig. 7d shows the statistical distribution of the vertical cross-section area of the struts as determined from 1456 struts. The histogram can be described by normal distribution with an average of 0.216 mm^2 which is 3.6% smaller than the target input area of 0.224 mm^2. In other words, the average strut diameter is only 524 μm instead of the targeted 534 μm. The statistical evaluation of the cross-section variations along the axis of individual struts yields an estimated surface roughness of $R_a = 20$ μm.

Fig. 8a shows a secondary electron (SE) image of the specimen's side. The strut shape appears to deviate from the target cylindrical shape due to some non-molten residual powder particles on the strut surfaces. Some porosity is visible on the strut surfaces as well as at the lattice nodes (see Fig. 8b). The EBSD is done on polished samples at two scales. Firstly, a step of 1.5 μm is used to analyze several unit cells. Fig. 10a shows a representative map of the [001] FCC crystal plane orientation. It becomes apparent that the polycrystalline structure of the SLM made truss lattice is highly heterogeneous. From a morphological point of view, it is worth noting that the struts feature highly elongated, up to 800 μm long grains that are aligned with the strut axes. We also observe significant differences between struts of different orientation (e.g. compare the ×45 and ×135 struts in Fig. 9a) which is tentatively attributed to differences in the temperature gradient during manufacturing. Within the nodes (strut intersections), two distinct regions are visible. The upper region features elongated grains that seem to follow the built-up direction of the lattice. The lower region on the other hand contains a lot of non-molten powder.

A higher resolution EBSD analysis with a step size of 0.3 μm is performed on selected regions to reveal the material texture. The inverse pole figure for a region of non-molten powder (Fig. 9b) shows a nearly isotropic grain orientation distribution, while the material within the struts is highly textured and dependent on the strut orientation (Fig. 9c and d).

5.2.2. Stress-strain response of the basis material

The true stress-strain curve obtained from in-situ SEM compression experiments on the mini-specimens is depicted as a solid red line in Fig. 10a. The reoccurring stress drops correspond to the relaxation of the material (and testing device) during SEM image acquisition. The measured Young's modulus is about 192 GPa and the yield stress at 0.2% plastic strain is 384 MPa. The large strain response is approximately linear with a hardening modulus of 1470 MPa.

The stress-strain response of the basis material as determined from static compression experiments on the larger standard specimens is significantly different. As shown in Fig. 10a (black curve), it features a yield stress of 530 MPa at a 0.2% plastic strain and hardening modulus of 1800 MPa over the strain interval [0.05, 0.20]. Even though the same alloy and SLM process has been

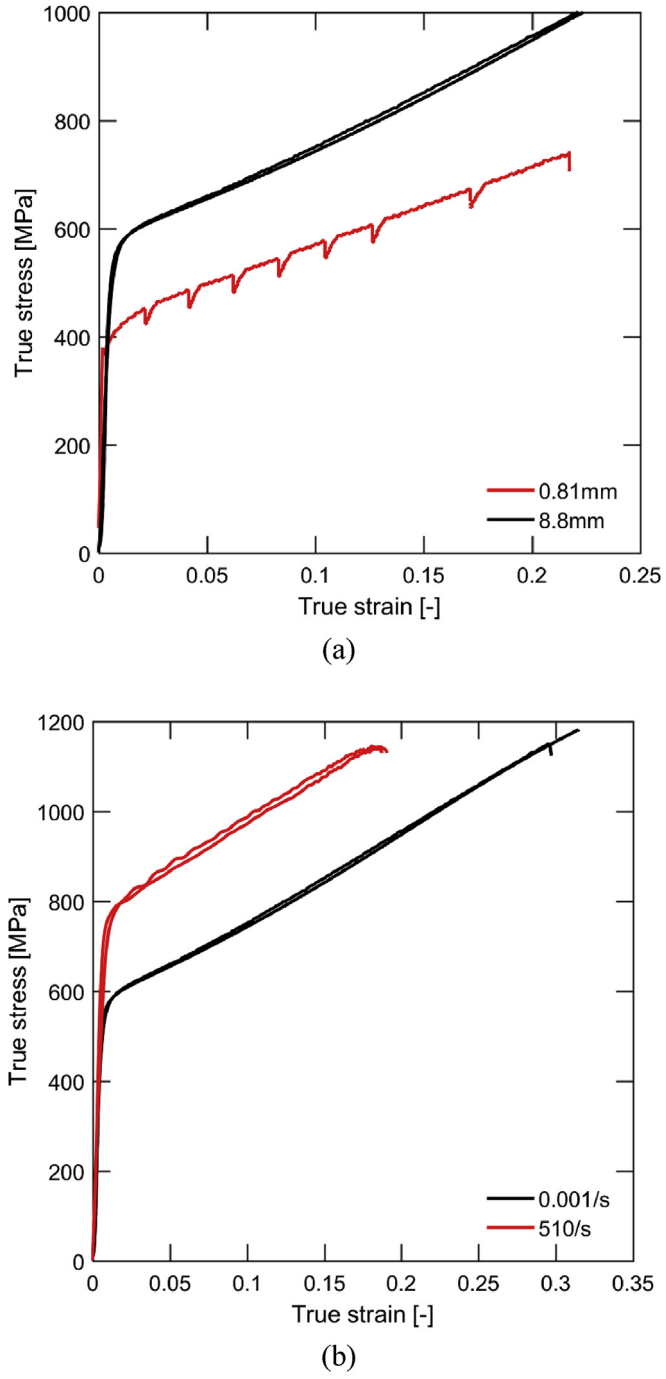

Fig. 10. Basis material stress-strain response. (a) effect of specimen size under static loading, (b) effect of strain rate.

employed to manufacture the specimens, it is noted that the grain structures are not identical in the mini- and standard-specimens due to different thermal gradients and temperature histories during manufacturing.

The SHPB experiments on the ring specimens (which inherited their microstructure from the standard specimens) are performed with a striker speed of 8.0 m/s. This resulted in an average true strain rate in the specimen of 510/s. The red curve in Fig. 10b shows the corresponding stress-strain curve for a representative dynamic experiment. The comparison with slow experiments on the standard cylinder specimens shows that the yield stress at a strain rate of the order of 10^3/s is almost 200 MPa higher than that at a strain rate of 10^{-3}/s, which corresponds to a Dynamic Increase Factor (DIF) of about 1.30 for the basis material. It is also noted that the dynamically loaded basis material specimens failed at a true compression strain of about −0.2 in a shear failure mode (probably due to adiabatic shear banding).

5.2.3. Stress-strain response of the micro-lattice material

The measured engineering stress-strain curve obtained from static compression experiments on the cubic micro-lattice specimens in shown in Fig. 11a. It features a plateau regime of an approximately constant stress of 50 MPa before densification at an engineering strain of about −0.49. The observed deformation mode is progressive crushing, i.e. the large plastic deformation begins at the specimen boundaries and then spreads towards the specimen center. Even though the material appears to collapse in a layer-by-layer fashion (Fig. 11b), the force-displacement curves does not exhibit any related high frequency oscillations. The experimental results also demonstrate that the plastic Poisson's ratio of the lattice material is close to zero.

The results from the high strain rate experiments on the cubic micro-lattice specimens are depicted in Fig. 12. All dynamic experiments on the lattice material are performed at a striker speed of 20 m/s. It exhibits the same features as the curve for static loading, i.e. a linear elastic regime, followed by a stress plateau prior to densification at a strain of about −0.56. The unloading/reloading cycle is due to the wave superposition in the input bar. The corresponding high speed photography images show the progressive crushing which begins at the output bar-specimen interface and progresses unilaterally until the entire specimen is crushed. The average macroscopic strain rate in these experiments is 1000 s^{-1}. The comparison with the low strain rate experiments (Fig. 11a) reveals a dynamic increase factor of 1.25.

The oscillations present in the results from SHPB experiments are mostly attributed to inaccuracies in the force measurement, however, we cannot rule out that wave reflections inside the lattice structure may also be partially responsible for oscillations the oscillations seen in Fig. 12.

6. Discussion

Our research has revealed that the mechanical properties of the basis material vary substantially within the SLM-made lattice structures. The comparison of the results for thin and thick SLM made structures (mini-versus standard specimen) reveals that the differences in grain morphology and texture (mostly due to different cooling conditions) can result in a yield stress difference of more than 20%

The experimental results on the prototype lattice material are in line with the results from the finite element study: in accordance with the design targets, the measured stress-strain curves for the lattice structure exhibits the desired plateau-like response between initial yield and the densification phase. We repeated the finite element simulation for a relative density of $\bar{\rho} = 0.27$ and the basis material properties as identified from the single strut experiments. The numerically-predicted plateau stress is with 46 MPa remarkably close that measured-experimentally. The observed plastic Poisson's ratio is close to zero which confirms another important feature of materials that are designed for energy absorption purposes.

The observed strain rate effect on the compressive response of the lattice material is very significant as far as the stress level is concerned. However, the dynamic increase factor of the truss lattice material is close to that of the basis material over the same range of strain rates. The rate effect in the lattice material response up to a

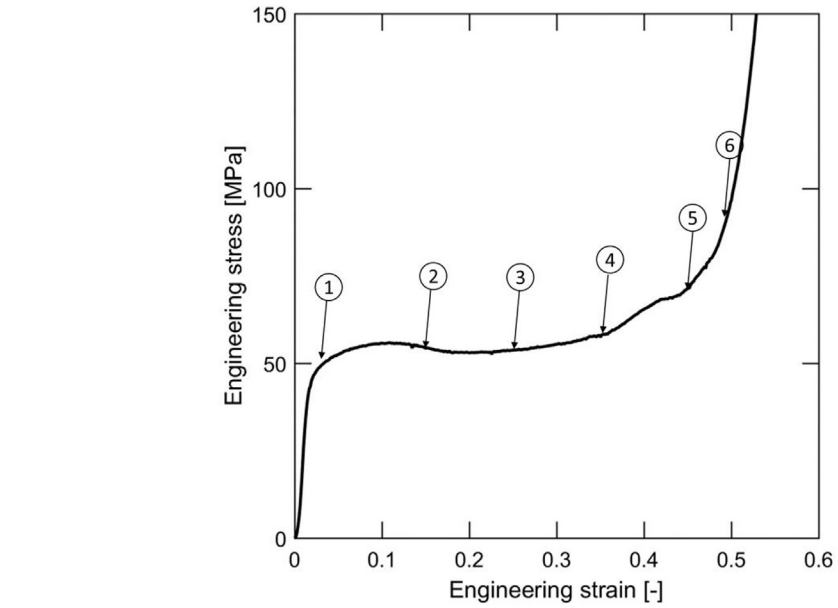

(a)

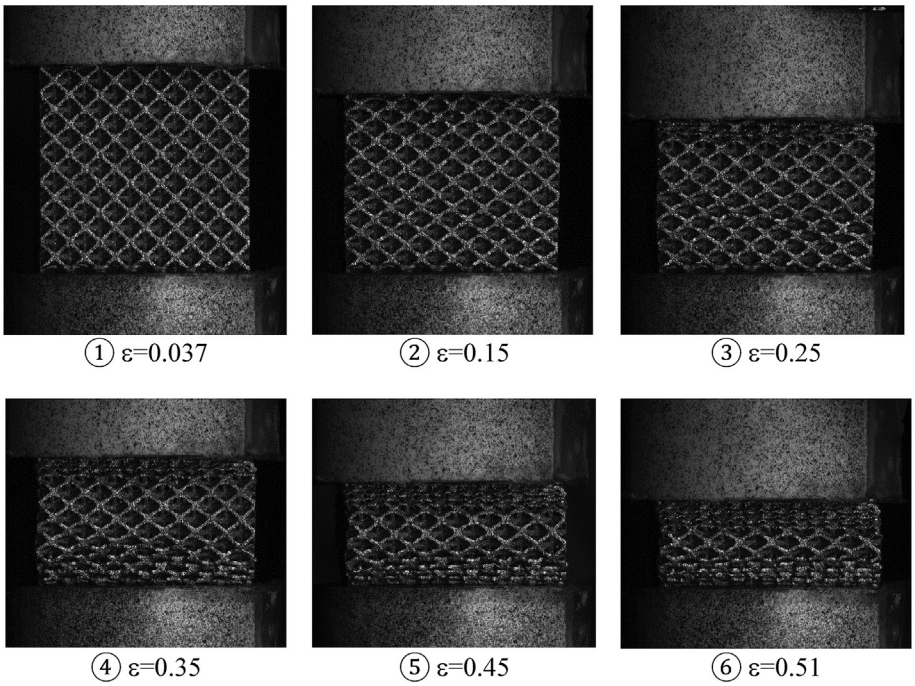

(b)

Fig. 11. Results from static compression experiments on truss lattice specimens with $\bar{\rho} = 0.27$: (a) Stress-strain curve and (b) selected deformed configurations.

strain rate of 1000/s is therefore entirely attributed to the rate-sensitivity in the basis material response. The small differences in the DIF (1.25 versus 1.30) are tentatively explained by the spatial heterogeneity of the strain rate field within the truss lattice structure.

Low density hexagonal honeycombs are often considered as the prime material for energy absorption purposes. The plateau stress for a thin-walled hexagonal honeycomb is related to the yield stress σ_0 of the basis material through the simple analytical approximation [26].

$$\sigma_p = 3.22\sigma_0\left(\frac{\rho}{\rho_s}\right)^{\frac{5}{3}}. \tag{10}$$

The relative specific energy absorption may thus be estimated as

$$\frac{\psi}{\psi_s} = 3.22\left(\frac{\rho}{\rho_s}\right)^{\frac{2}{3}}. \tag{11}$$

The comparison with Eq. (7) suggests that the specific energy absorption of the lattice material with solid struts is significantly

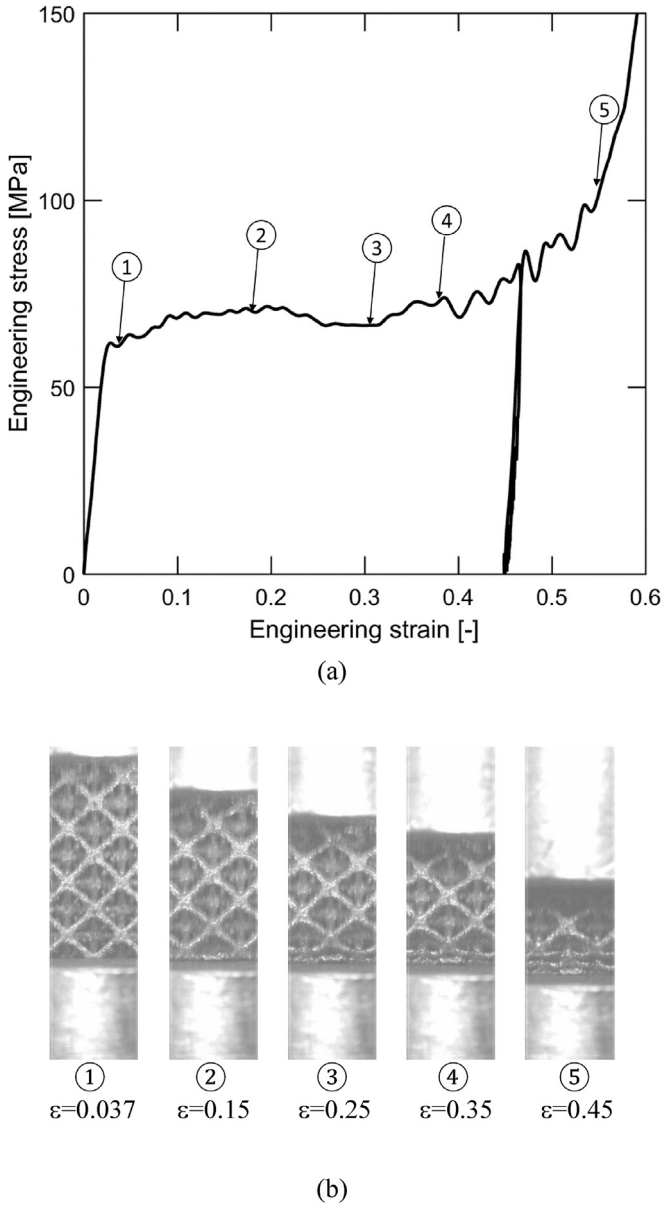

Fig. 12. Results from dynamic compression experiments at 20 m/s on truss lattice specimens with $\bar{\rho} = 0.27$: (a) Stress-strain curve and (b) selected deformed configurations.

lower than that of honeycomb made from the same basis material and of the same relative density.

According to our numerical simulations, the 30% relative density lattice has a relative SEA of $\frac{\psi}{\psi_s} \cong 0.38$. Its specific energy absorption is therefore higher than that of honeycombs of relative densities below 4%. Given that most commercially available metallic honeycombs have relative densities of less than 5%, the use of high density lattice materials may provide a viable alternative in engineering practice. In particular, the lattice material provides the high energy absorption capability for any loading direction, while the performance of a honeycomb brakes significantly down in case it is loaded off-axis.

7. Conclusions

The mechanical behavior of stainless steel 316L octet truss lattice materials made through selective laser melting is investigated. The main conclusions drawn from this combined numerical and experimental study are:

1. The macroscopic large strain compression response of the octet truss lattice material becomes stable at relative densities above 30%. In other words, the stress-strain response is a monotonically increasing function if the porosity is smaller than 70%,
2. The specific energy absorption (SEA) of lattice materials is a monotonically increasing function of the relative density. For the specific stainless steel lattices with a plateau-like stress-strain response prior to densification, the SEA was about 30% of the SEA of the basis material. This percentage is significantly higher than that for conventional thin-walled honeycomb structures.
3. The shape of the constituting straight truss members plays an important role as far as the overall stress-strain response is concerned. It is found that slightly tapered axisymmetric trusses (ratio of min. to max. strut diameter of 0.8) provide the highest macroscopic yield strength. It is worth noting that the performance of lattice structures with cylindrical struts is close to that of the optimum truss geometry.
4. 27% relative density lattice materials of 2.2 mm strut length and 500μm average strut diameter have been manufactured using Selective Laser Melting (SLM). Aside from a poor surface roughness of $R_a = 20$ μm, EBSD analysis revealed significant spatial variations in the grain morphology and texture within the lattice structure.
5. Experiments on SLM made cylindrical specimens of different diameter revealed that the yield strength of can increase by nearly 50% when increasing the specimen diameter from 0.8 to 8 mm. This effect is attributed to differences in the temperature history during manufacturing that results in very different polycrystalline microstructures.
6. The apparent strength of the lattice material increased by about 30% when increasing the strain rate from 10^{-3}/s to 10^{3}/s. This effect is attributed to the strain rate sensitivity of the basis material.

Acknowledgements

The authors are grateful to Mr. Alexandre Tanguy, Mr. Simon Hallais, Mr. Philippe Chevalier and Prof. Gerard Gary from the Laboratoire de Mecanique des Solides (LMS, Ecole Polytechnique, France), Prof. Michel Bornert and Dr. Patrick Aimedieu (Laboratoire Navier, ENPC, France) for their outstanding support of our experimental work. Thanks are also due to Dr. Christian Roth (ETH), Mr. Colin Bonatti (ETH/MIT) and Prof. Tomasz Wierzbicki (MIT) for valuable discussions. Seed funding from Exxon Mobil under Grant #023730-00017 is also gratefully acknowledged.

References

[1] V.S. Deshpande, M.F. Ashby, N.A. Fleck, Foam topology: bending versus stretching dominated architectures, Acta Mater. 49 (2001a) 1035–1040.
[2] T.A. Schaedler, A.J. Jacobsen, A. Torrents, A.E. Sorensen, J. Lian, J.R. Greer, et al., Ultralight metallic microlattices, Science 334 (2011) 962–965.
[3] X. Wendy Gu, J.R. Greer, Ultra-strong architected Cu meso-lattices, Extrem. Mech. Lett. 2 (2015) 7–14.
[4] J. Bauer, S. Hengsbach, I. Tesari, R. Schwaiger, O. Kraft, High-strength cellular ceramic composites with 3D microarchitecture, Proc. Natl. Acad. Sci. U. S. A. 111 (2014) 2453–2458.
[5] X. Zheng, H. Lee, T.H. Weisgraber, M. Shusteff, J. DeOtte, E.B. Duoss, et al., Ultralight, ultrastiff mechanical metamaterials, Science 344 (2014) 1373–1377.
[6] Fuller, R.B., 1961. Octet truss. U.S. Patent Serial No. 2, 986, 241.
[7] V.S. Deshpande, N. a. Fleck, M.F. Ashby, Effective properties of the octet-truss lattice material, J. Mech. Phys. Solids 49 (2001b) 1747–1769.
[8] D. Mohr, Mechanism-based multi-surface plasticity model for ideal truss lattice materials, Int. J. Solids Struct. 42 (2005) 3235–3260.

[9] A. Vigliotti, V.S. Deshpande, D. Pasini, Nonlinear constitutive models for lattice materials, J. Mech. Phys. Solids 64 (2014) 44–60.
[10] M.C. Messner, M.I. Barham, M. Kumar, N.R. Barton, Wave propagation in equivalent continuums representing truss lattice materials, Int. J. Solids Struct. 73–74 (2015) 55–66.
[11] H.N.G. Wadley, N.A. Fleck, A.G. Evans, Fabrication and structural performance of periodic cellular metal sandwich structures, Compos. Sci. Technol. 63 (2003) 2331–2343.
[12] D.J. Sypeck, H.N.G. Wadley, Multifunctional microtruss laminates: textile synthesis and properties, J. Mater. Res. 16 (2012) 890–897.
[13] L. Dong, V. Deshpande, H. Wadley, Mechanical response of Ti–6Al–4V octet-truss lattice structures, Int. J. Solids Struct. 60–61 (2015) 107–124.
[14] D. Queheillalt, V. Deshpande, H. Wadley, Truss waviness effects in cellular lattice structures, J. Mech. Mater. Struct. 2 (2007) 1657–1675.
[15] R. Gümrük, R.A.W. Mines, Compressive behaviour of stainless steel micro-lattice structures, Int. J. Mech. Sci. 68 (2013) 125–139.
[16] R. Gümrük, R.A.W. Mines, S. Karadeniz, Static mechanical behaviours of stainless steel micro-lattice structures under different loading conditions, Mater. Sci. Eng. A 586 (2013) 392–406.
[17] R.A.W. Mines, S. Tsopanos, Y. Shen, R. Hasan, S.T. McKown, Drop weight impact behaviour of sandwich panels with metallic micro lattice cores, Int. J. Impact Eng. 60 (2013) 120–132.
[18] X. Tang, V. Prakash, J.J. Lewandowski, G.W. Kooistra, H.N.G. Wadley, Inertial stabilization of buckling at high rates of loading and low test temperatures: implications for dynamic crush resistance of aluminum-alloy-based sandwich plates with lattice core, Acta Mater. 55 (2007) 2829–2840.
[19] S. Li, H. Hassanin, M.M. Attallah, N.J.E. Adkins, K. Essa, The development of TiNi-based negative Poisson's ratio structure using selective laser melting, Acta Mater. 105 (2016) 75–83.
[20] S.J. Li, L.E. Murr, X.Y. Cheng, Z.B. Zhang, Y.L. Hao, R. Yang, et al., Compression fatigue behavior of Ti–6Al–4V mesh arrays fabricated by electron beam melting, Acta Mater. 60 (2012) 793–802.
[21] Z. Ozdemir, E. Hernandez-Nava, A. Tyas, J.A. Warren, S.D. Fay, R. Goodall, et al., Energy absorption in lattice structures in dynamics: experiments, Int. J. Impact Eng. 89 (2015) 49–61.
[22] H.N.G. Wadley, Cellular metals manufacturing, Adv. Eng. Mater. 4 (2002) 726–733.
[23] M.S.A. Elsayed, D. Pasini, Multiscale structural design of columns made of regular octet-truss lattice material, Int. J. Solids Struct. 47 (2010) 1764–1774.
[24] A.G. Evans, M.Y. He, V.S. Deshpande, J.W. Hutchinson, A.J. Jacobsen, W.B. Carter, Concepts for enhanced energy absorption using hollow micro-lattices, Int. J. Impact Eng. 37 (2010) 947–959.
[25] R. Othman, G. Gary, Testing aluminum alloy from quasi-static to dynamic strain-rates with a modified Split Hopkinson bar method, Exp. Mech. 47 (2007) 295–299.
[26] T. Wierzbicki, Crushing analysis of metal honeycombs, Int. J. Impact Eng. 1 (1983) 157–174.
[27] A.B. Spierings, G. Levy, Comparison of density of stainless steel 316L parts produced with selective laser melting using different powder grades, in: Proceedings of the Annual International Solid Freeform Fabrication Symposium. Austin, Texas, 342–353, 2009.
[28] D. Mohr, G. Gary, B. Lundberg, Evaluation of stress-strain curve estimates in dynamic experiments, Int. J. Impact Eng. 37 (2) (2010) 161–169.